Different Low-Frequency (1/*f*) Noise Origins in Atomically Thin ALD In_2O_3 TFTs Determined by the Quantum-Confinement Effect

Sumi Lee, Jian-Yu Lin, Chang Niu, Chun-An Shih, Linjia Long, Muhammad A. Alam, and Peide D. Ye*
Elmore Family School of Electrical and Computer Engineering, Purdue University, West Lafayette, IN, U.S.A.
*Email: yep@purdue.edu

Abstract Low-frequency (1/*f*) noise in amorphous-oxide-semiconductor (AOS) TFTs increases as device area scales down, but its origin is obscured by misleading S_{ID}/I_D^2–V_{OV} slopes. Using ultrathin atomic-layer-deposited (ALD) In_2O_3 TFTs that span channel degeneracy and contact barriers (2 nm: degenerate, $\varphi_{SBH} < 0$; 1.2 nm: nondegenerate, $\varphi_{SBH} > 0$), we combine temperature-dependent S_{VG} with Dutta-Horn analysis and cleanly separate two regimes: the 2 nm devices follow tunneling-assisted carrier-number fluctuations (ΔN) ($\alpha \approx 1$, nearly flat $D(E_a)$), whereas the 1.2 nm devices exhibit $\alpha < 1$ with a redistributed $D(E_a)$, implicating band-tail-coupled ΔN. Finally, *bias*- and L_{ch}-scaling reveal a transition to contact-noise dominance at high V_{OV} only in the 1.2 nm devices.

I. Introduction

A literature mapping of AOS low-frequency noise (LFN) in **Fig. 1(a)** shows a clear collapse of normalized drain-current noise power spectral density (S_{ID}/I_D^2) ∝ 1/*Area* across reported AOS TFTs [1]-[9], implying an unavoidable noise penalty as device footprint shrinks–an emerging concern for BEOL-compatible logic and sensing platforms where low-frequency fluctuations directly degrade operating-point stability and variability margins. Despite this consensus in scaling, the microscopic origin remains unsettled, in part because many studies still rely heavily on the S_{ID}/I_D^2–V_{OV} slope analysis to distinguish carrier-number (CNF) [10] and mobility (MF) fluctuation [11]. A recent study on scaled Si MOSFETs reported elevated 1/*f* noise upon lowering the temperature (*T*) [12]. These results contrast with the conventional CNF picture, where tunneling-mediated channel–oxide trap exchange drives carrier-number fluctuations (ΔN) and the resulting flat-band-equivalent gate-bias fluctuations (ΔV_{fb}) tend to weaken as *T* decreases (**Fig. 2(b)**, left) [10]. This discrepancy suggests an additional $\Delta N/\Delta V_{fb}$ source, whose active ensemble evolves with *T*, as illustrated by the Dutta-Horn (DH)-type picture in **Fig. 2(b)** (right) [13]. In this work, we use atomically thin ALD In_2O_3 TFTs (1.2 nm vs. 2 nm) as a controlled platform in which varying the channel thickness concurrently tunes the channel degeneracy and the contact barrier height (φ_{SBH}), and we present a physics-consistent LFN interpretation by combining *bias*-, *T*-, and channel length (L_{ch})-scaling analyses.

II. Device Fabrication and Measurement Setup

Bottom-gated In_2O_3 TFTs were fabricated with a 4-nm ALD HfO_2 gate dielectric, without a post-deposition thermal anneal. The channel thickness was set to 1.2 nm and 2 nm, deposited by ALD at 200 °C. Detailed fabrication steps are provided in [14]. The noise characteristics were measured using Keysight E4727A ALFNA, and *T*-dependent measurements were performed in a Lakeshore CRX-VF cryogenic probe station.

III. Results and Discussion

A. Limitations of V_{OV}-Slope Diagnosis

Figs. 3(a)–(b) show S_{ID}/I_D^2 for the 1.2 nm and 2 nm In_2O_3 TFTs over $V_{OV} = V_{GS}–V_T = 0$–3.3 V, both exhibiting clear 1/*f* spectra. **Fig. 3(c)** plots S_{ID}/I_D^2 at 100 Hz versus V_{OV}; notably, no single slope (e.g., −1 or −2) is observed. In CNF, $S_{ID}/I_D^2 = (g_m/I_D)^2 S_{Vfb}$; thus, an apparent −2 requires an ideal $(g_m/I_D) \propto 1/V_{OV}$ scaling [10]. As shown in **Fig. 3(d)**, however, $(g_m/I_D)^2$ is strongly V_{OV}-dependent and closely tracks the measured S_{ID}/I_D^2 over the bias range. This result indicates that S_{ID}/I_D^2–V_{OV} slope diagnosis is unreliable unless $(g_m/I_D)^2$ is explicitly accounted for. Nevertheless, in the low-V_{OV} regime, $S_{ID}/I_D^2 \propto (g_m/I_D)^2$ holds regardless of channel thickness, suggesting a ΔN origin for the channel noise. In the following, we use g_m-normalized and *T*-dependent analyses to identify the active states governing ΔN, focusing on the channel-noise-dominated (low-V_{OV}) regime.

B. Temperature Dependence of Input-Referred LFN (S_{VG})

Figs. 4−5 compare the *T*-dependence of 1/*f* noise. For 2 nm, S_{ID}/I_D^2 decreases as *T* is lowered (**Fig. 4(a)**), while $(g_m/I_D)^2$ changes only modestly (**Fig. 4(b)**). We use the input-referred noise $S_{VG} = S_{ID}/g_m^2$ to remove the explicit transconductance factor. In **Figs. 4(c)–(d)**, S_{VG} decreases monotonically with decreasing *T*, consistent with the CNF picture. By contrast, for 1.2 nm, both S_{ID}/I_D^2 and S_{VG} increase as *T* decreases (**Figs. 5(a)**, **5(c)**), and the increase persists across the measured *f* range (**Fig. 5(d)**). This *opposite* trend points to an additional ΔN pathway beyond pure tunneling-assisted CNF. We therefore examine the spectral exponent α and extract $D(E_a)$ to test consistency with a DH-type spectrum.

C. Evidence for Band-Tail-Coupled LFN at Low *T*

We quantify spectral deviation using the exponent α in $1/f^{\alpha}$ and extract the activation-energy distribution $D(E_a)$ within the DH framework [13]. For 2 nm, S_{VG} remains close to ideal 1/*f* from 300 K down to 60 K (**Fig. 6(a)**), with $\alpha \approx 1$ over the full *T* range for both L_{ch} = 1 µm and 0.1 µm (**Fig. 6(b)**), consistent with tunneling-assisted CNF. In great contrast, the 1.2 nm device exhibits a clear low-*T* deviation from 1/*f* with $\alpha < 1$ (**Fig. 6(c)–6(d)**). In DH theory, each source of fluctuation follows $\tau = \tau_0 \exp(E_a/k_B T)$, and a given *f* predominantly samples processes satisfying $\omega\tau \sim 1$; thus, $\alpha \neq 1$ implies a non-uniform effective $D(E_a)$ within the sampled E_a window.

Figs. 7(a)–(b) show the $T \leftrightarrow E_a$ mapping of $D(E_a)$ at different V_{OV}, and **Figs. 7(c)–(d)** replot the normalized $D(E_a)$ versus E_a across *f*. The 2 nm devices exhibit a nearly energetically uniform $D(E_a)$ ($\propto 1/k_B T$) across the bias range. By contrast again, the 1.2 nm devices show (i) a pronounced redistribution near $T \approx 150$ K and (ii) strong weighting toward low E_a, suggesting enhanced participation of near-band-edge (band-tail-coupled) active states. This crossover coincides with the onset of SS degradation extracted from the I_D–V_G characteristics (**Figs. 8(b)–(c)**). **Fig. 8(a)** provides a physical model: in the degenerate 2 nm channel, the trap neutrality level (TNL) lies above E_c, leaving acceptor-like tail states in the bandgap largely occupied and weakly charge-state active; whereas in the nondegenerate 1.2 nm channel, quantum confinement shifts the TNL inside the bandgap [15], rendering these tail states partially charge-state active and enabling band-tail-coupled trap exchange.

D. Breakdown of g_m-Scaling: Transition to Contact Noise

At high V_{OV} (> 1 V), S_{ID}/I_D^2 in the nondegenerate 1.2 nm device deviates from $(g_m/I_D)^2$ scaling and saturates versus V_{OV}, while $S_{ID} \propto I_D^2$ for both long and short L_{ch} (**Figs. 9–10**), consistent with multiplicative series-resistance modulation [16]. This behavior is absent in the degenerate 2 nm devices, which remain channel-noise dominated over the same bias range. The DC resistance partition further highlights the contrast: for 2 nm, $(R_c/R_{tot})^2$ is nearly V_{OV}-independent across L_{ch} (**Figs. 10(c)**), whereas for 1.2 nm it increases with V_{OV} and grows strongly as L_{ch} scales, exceeding $(R_{ch}/R_{tot})^2$ in the 100 nm regime (**Figs. 10(d)**). Importantly, **Eq. (1)** shows that the observed plateau cannot be explained by the DC partition alone. The S_{ID}/I_D^2 saturation persists even in long L_{ch} when $(R_c/R_{tot})^2 < (R_{ch}/R_{tot})^2$, indicating that the dominance is driven by a larger intrinsic $S_{R,c}$ ($\gg S_{R,ch}$), not only a larger R_c fraction (**Fig. 11(a)**). This stronger contact contribution in the 1.2 nm devices is consistent with a more rectifying metal/AOS contact ($\varphi_{SBH} > 0$) compared to 2 nm devices ($\varphi_{SBH} < 0$) as reported in [15], corroborated by the larger R_c in **Fig. 11(b)**. Moreover, the V_D dependence observed only at low *f* suggests an E_a-dependent contact-related fluctuation component (**Figs. 11(c)–(d)**).

IV. Conclusion

In this work, we show that the apparent S_{ID}/I_D^2–V_{OV} slope is not a reliable fingerprint in scaled AOS TFTs because it largely reflects the $(g_m/I_D)^2$ scaling, consistent with trap-exchange-driven channel noise (ΔN, observed as an equivalent ΔV_{fb}). Thickness- and temperature-dependent Dutta-Horn analyses further reveal a shift in the dominant trap-exchange pathway: 2 nm (degenerate) In_2O_3 follows a tunneling-assisted CNF picture, whereas 1.2 nm (nondegenerate) exhibits band-tail-coupled exchange with concomitant quantum-confinement-induced TNL realignment, yielding an energy-dependent DH spectrum. Finally, in the scaled channel length (L_{ch} < 1 µm), barrier-limited contacts ($\varphi_{SBH} > 0$) can drive a transition to contact-noise dominance, where a larger intrinsic $S_{R,c}$–not DC R_c/R_{tot} partition–governs S_{ID}/I_D^2 and results in a plateau versus V_{OV}. Practically, band-tail-state density and contact stability emerge as dual design knobs for LFN in scaled AOS TFTs.

Acknowledgements: This work is supported by NSF FuSe2, SRC GRC, and Samsung Electronics, Inc.

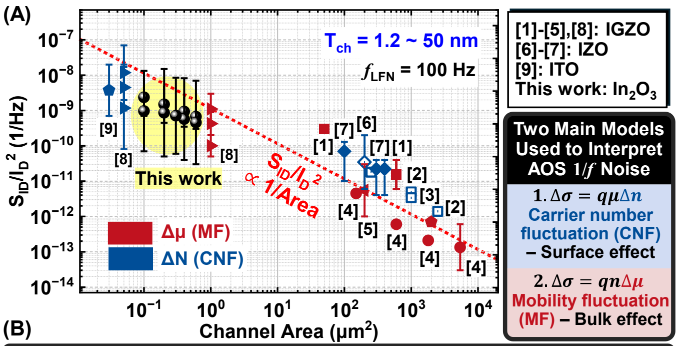

Key Open Problems in Understanding AOS 1/f Noise

- ❑ Existing AOS LFN studies lack a unified interpretation, as CNF and MF models have been used inconsistently.
- ❑ This uncertainty is compounded by the fact that AOS LFN, despite large channel thickness variations, collapses onto a universal 1/Area trend.
- ❑ Therefore, the true origin of 1/f noise in AOS channels — especially in scaled, contact-limited devices — remains unresolved.

Fig. 1. (a) Reported AOS 1/*f* noise versus channel area, including this work's ultra-thin In_2O_3 devices, showing a universal 1/Area trend. (b) Key open problems in AOS 1/*f* noise, highlighting inconsistent CNF/MF usage and the unresolved origin in scaled AOS channels.

(A) Highlights of this work

1. First to point out that slope-based CNF/MF diagnosis fails in AOS; $S_{ID}/I_D^2 \propto g_m^2/I_D^2$ provides the correct CNF signature.
2. Temperature-dependent measurements reveal that a TNL shift drives a transition from tunneling-dominated to band-tail–induced 1/*f* noise in ultra-thin In_2O_3.
3. L_{ch} scaling clarifies the competing roles of S_{ch} and S_c, showing that S_c can dominate the 1/*f* noise even when R_c contributes less to R_{tot} than R_{ch}.

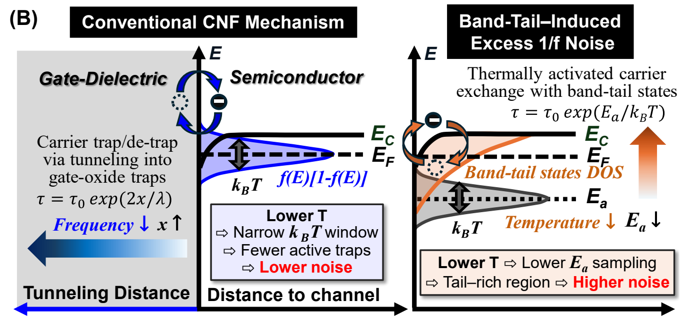

Fig. 2. (a) Summary of the key findings. (b) Schematic comparison of two 1/*f* noise mechanisms: (left, CNF model) governed by tunneling-driven carrier exchange with gate-oxide traps, and (right, DH model) governed by thermally activated carrier exchange with band-tail states.

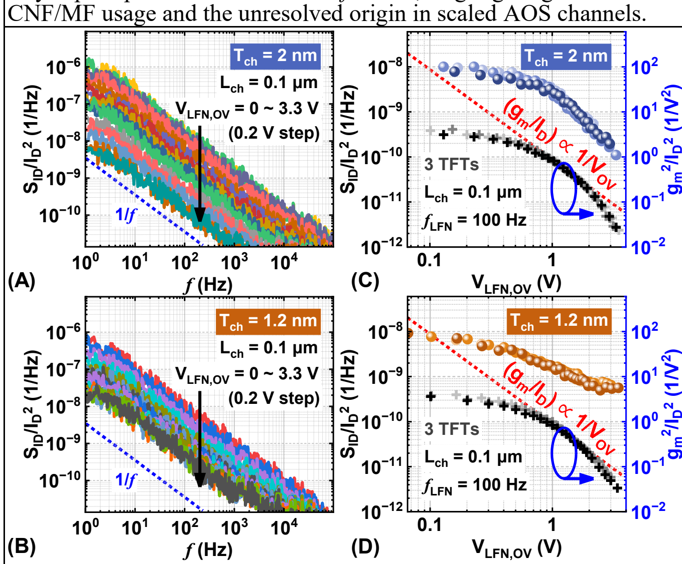

Fig. 3. S_{ID}/I_D^2 versus frequency of (a) 2 nm and (b) 1.2 nm In_2O_3 TFTs. S_{ID}/I_D^2 and $(g_m/I_D)^2$ versus V_{OV} (= 0.06 V ~ 4 V) for (c) 2 nm and (d) 1.2 nm, with the red dashed line showing the ideal $g_m/I_D \propto 1/V_{OV}$ dependence. At least three TFTs are measured for each condition.

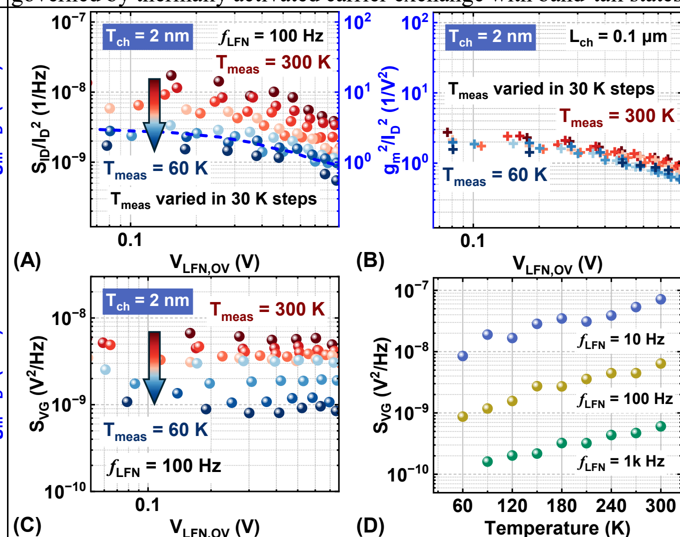

Fig. 4. (a) S_{ID}/I_D^2, $(g_m/I_D)^2$ (@ 300 K), and (b) $(g_m/I_D)^2$ versus V_{OV} for 2 nm In_2O_3 TFTs measured from 300 K to 60 K. (c) S_{VG} (= S_{ID}/g_m^2) versus V_{OV}. (d) S_{VG} as a function of temperature for multiple f_{LFN} (= 10~1000 Hz), showing a *decrease* of 1/*f* noise at lower temperature.

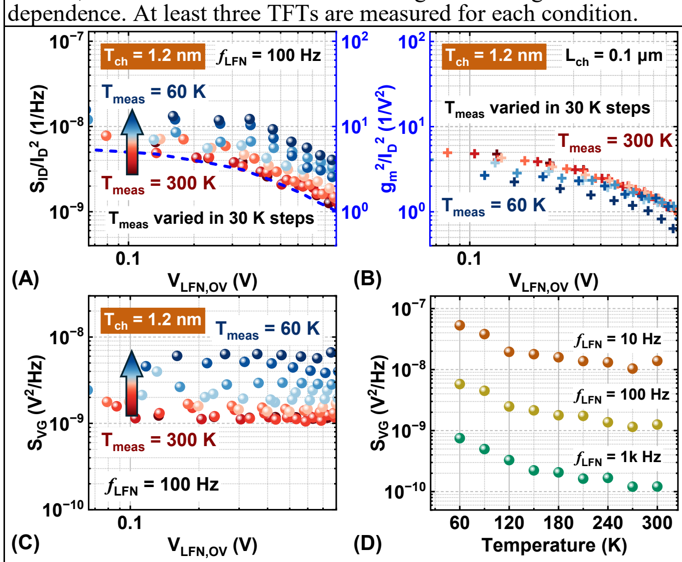

Fig. 5. (a) S_{ID}/I_D^2, $(g_m/I_D)^2$ (@ 300 K), and (b) $(g_m/I_D)^2$ versus V_{OV} for 1.2 nm In_2O_3 TFTs measured from 300 K to 60 K. (c) S_{VG} (= S_{ID}/g_m^2) versus V_{OV}. (d) S_{VG} as a function of temperature for multiple f_{LFN} (= 10~1000 Hz), showing an *increase* in 1/*f* noise at lower temperature.

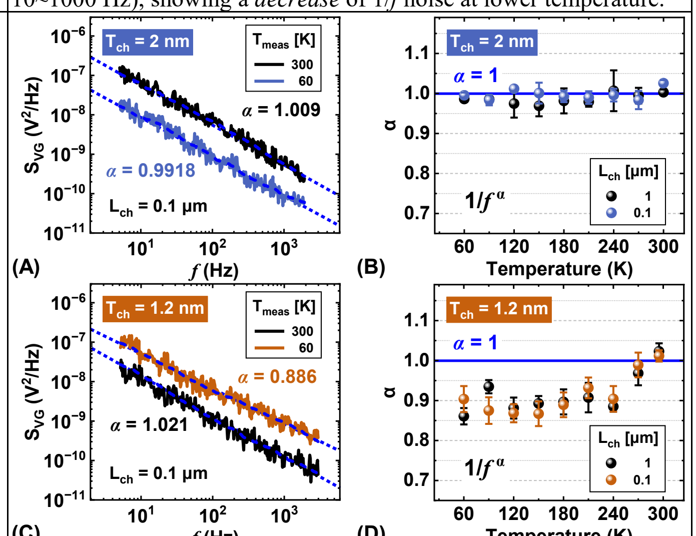

Fig. 6. S_{VG} versus frequency for (a) 2 nm and (c) 1.2 nm In_2O_3 TFTs at 300 K and 60 K, used to extract the frequency exponent α ($1/f^{\alpha}$). α versus temperature for (b) 2 nm and (d) 1.2 nm devices, showing deviation from α = 1 at low temperature only in the 1.2 nm device.

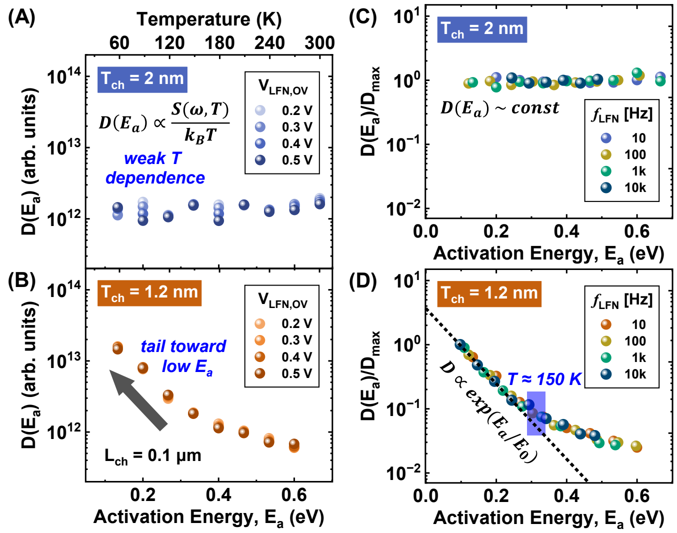

Fig. 7. (a–b) DH-extracted activation-energy distribution $D(E_a)$ plotted with the T ↔ E_a mapping at f_{LFN} = 10 Hz for multiple V_{OV} in 2 nm and 1.2 nm In_2O_3 TFTs. (c–d) $D(E_a)$ normalized to its peak value and replotted versus E_a at various f_{LFN} (L_{ch} = 0.1 μm).

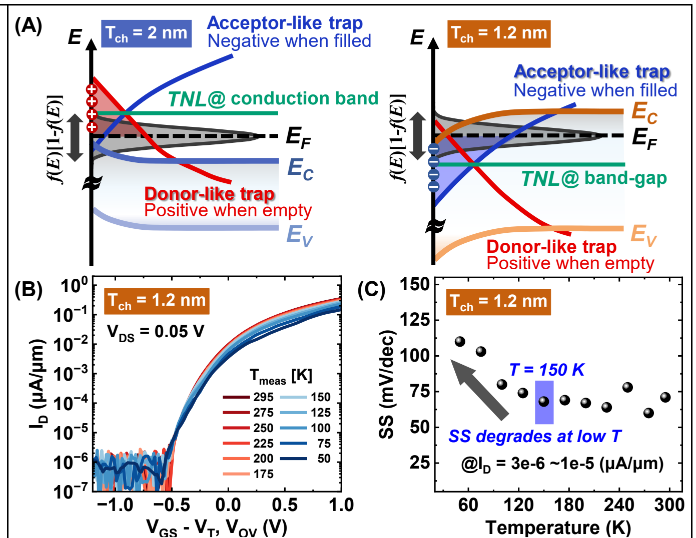

Fig. 8. (a) Conceptual illustration of the TNL location in 2 nm and 1.2 nm In_2O_3 at the same V_{OV}, with the grey region indicating the active energy window. (b) T-dependent I_D–V_{OV} characteristics of 1.2 nm In_2O_3 TFTs (L_{ch} = 1 μm) and (c) extracted SS as a function of T.

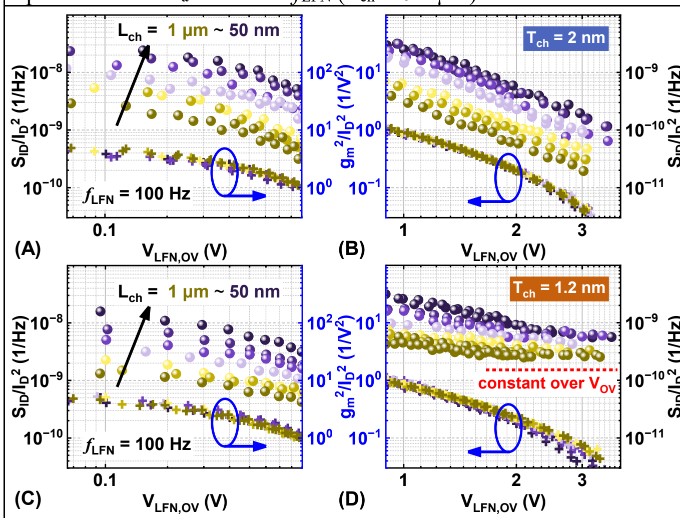

Fig. 9. S_{ID}/I_D^2 and $(g_m/I_D)^2$ versus V_{OV} for In_2O_3 TFTs with channel lengths from 1 μm to 50 nm: (a-b) 2 nm and (c-d) 1.2 nm. (a, c) show the low-V_{OV} region (< 1 V), while (b, d) show the high-V_{OV} (≥ 1 V) region. A saturation-like behavior in S_{ID}/I_D^2 at the high V_{OV} region appears only in the 1.2 nm devices.

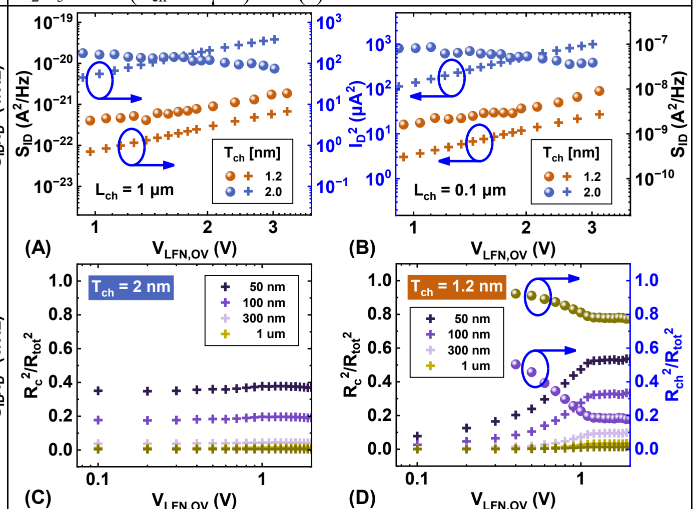

Fig. 10. S_{ID} and I_D^2 versus V_{OV} for In_2O_3 TFTs with L_{ch} of (a) 1 μm and (b) 0.1 μm, showing that $S_{ID} \propto I_D^2$ occurs only in the 1.2 nm devices. (c) Extracted $(R_c/R_{tot})^2$ versus V_{OV} for 2 nm over L_{ch} = 1 μm–50 nm, showing near V_{OV}-independence. (d) $(R_c/R_{tot})^2$ and $(R_{ch}/R_{tot})^2$ versus V_{OV} for 1.2 nm devices over the same L_{ch} range.

Eq. (1)

$$\frac{S_{ID}}{I_D^2} = \frac{S_R}{R^2} = \frac{S_{R,ch}}{R_{ch}^2} \cdot \frac{R_{ch}^2}{R_{tot}^2} + \frac{S_{R,c}}{R_c^2} \cdot \frac{R_c^2}{R_{tot}^2}$$

Table. I

	Lower V_{OV}	Higher V_{OV}
T_{ch} = 1.2 nm	$S_{ch} \gg S_c$	$S_{ch} \ll S_c$
T_{ch} = 2 nm	$S_{ch} \gg S_c$	$S_{ch} \gg S_c$

(A)

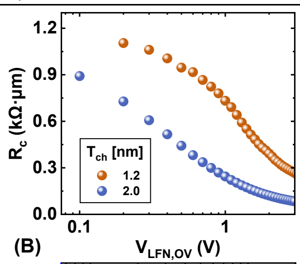

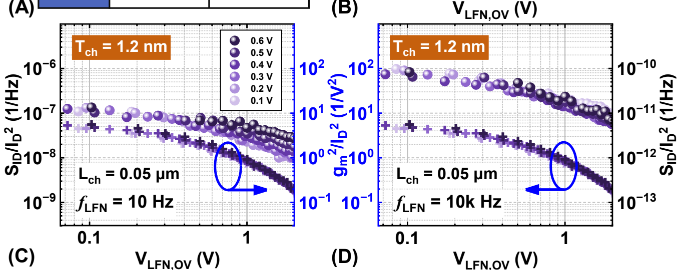

Fig. 11. (a) Summary of the $S_{R,ch}$–$S_{R,c}$ competition extracted from series resistance decomposition for 1.2 nm and 2 nm channels. (b) Extracted R_c versus V_{OV} for 1.2 nm and 2 nm devices (R_c is extracted by TLM). V_D-dependent S_{ID}/I_D^2 and $(g_m/I_D)^2$ versus V_{OV} for 1.2 nm In_2O_3 TFTs with L_{ch} = 50 nm at (c) f_{LFN} = 10 Hz and (d) f_{LFN} = 10 kHz.

References

[1] I. -T. Cho *et al.*, *IEEE Electron Device Letters*, vol.30, no.8, pp. 828, 2009, doi: 10.1109/LED.2009.2023543. [2] H. -S. Choi *et al.*, *IEEE Electron Device Letters*, vol. 32, no. 8, pp. 1083, 2011, doi: 10.1109/LED.2011.2158057. [3] R. Vatsyayan *et al.*, *IEEE Transactions on Electron Devices*, vol.70, no.9, pp. 4647, 2023, doi: 10.1109/TED.2023.3284803. [4] T.-C. Fung *et al.*, *Journal of Applied Physics*, 108, 074518, 2010, doi: 10.1063/1.3490193. [5] Y. Chen *et al.*, *IEEE Journal of the Electron Devices Society*, vol.12, pp. 275, 2024, doi: 10.1109/JEDS.2024.3375867. [6] Y. Chen *et al.*, *Applied Physics Letters*, 124, 173507, 2024, doi: 10.1063/5.0204316. [7] Y. Liu *et al.*, *IEEE Journal of the Electron Devices Society*, vol.6, pp. 271, 2018, doi: 10.1109/JEDS.2018.2800049. [8] S. Lee *et al.*, *IEEE Transactions on Electron Devices*, vol.72, no.6, pp. 2993, 2025, doi: 10.1109/TED.2025.3562509. [9] C. Gu *et al.*, *Applied Physics Letters*, 122, 252104, 2023, doi: 10.1063/5.0147577. [10] A. L. McWhorter, *ed. R. H. Kingston, University of Pennsylvania Press*, pp. 207, 1957, doi: N/A. [11] F. N. Hooge, *IEEE Transactions on Electron Devices*, vol. 41, no. 11, pp. 1926-1935, 1994, doi: 10.1109/16.333808. [12] R. Asanovski *et al.*, *IEEE IEDM*, 2022, doi: 10.1109/IEDM45625.2022.10019388. [13] P. Dutta *et al.*, *Reviews of Modern Physics*, 53, 497, 1981, doi: 10.1103/RevModPhys.53.497. [14] J.-Y. Lin *et al.*, *IEEE Transactions on Electron Devices*, vol.72, no.6, pp. 3004, 2025, doi: 10.1109/TED.2025.3564265. [15] J. -Y. Lin *et al.*, *IEEE IEDM*, 2024, pp. 1-4, doi: 10.1109/IEDM50854.2024.10873514. [16] C. J. Delker *et al.*, *IEEE Transactions on Electron Devices*, vol. 60, no. 9, pp. 2900, 2013, doi: 10.1109/TED.2013.2274009.